ARTICLES
PUBLISHED ONLINE: 25 JANUARY 2016 | DOI: 10.1038/NMAT4555
nature materials

Interfacial electronic effects control the reaction selectivity of platinum catalysts

Guangxu Chen[1,2†], Chaofa Xu[1,2†], Xiaoqing Huang[1,2], Jinyu Ye[1], Lin Gu[3], Gang Li[4], Zichao Tang[4], Binghui Wu[1,2], Huayan Yang[1,2], Zipeng Zhao[1,2], Zhiyou Zhou[1], Gang Fu[1,2*] and Nanfeng Zheng[1,2*]

Tuning the electronic structure of heterogeneous metal catalysts has emerged as an effective strategy to optimize their catalytic activities. By preparing ethylenediamine-coated ultrathin platinum nanowires as a model catalyst, here we demonstrate an interfacial electronic effect induced by simple organic modifications to control the selectivity of metal nanocatalysts during catalytic hydrogenation. This we apply to produce thermodynamically unfavourable but industrially important compounds, with ultrathin platinum nanowires exhibiting an unexpectedly high selectivity for the production of *N*-hydroxylanilines, through the partial hydrogenation of nitroaromatics. Mechanistic studies reveal that the electron donation from ethylenediamine makes the surface of platinum nanowires highly electron rich. During catalysis, such an interfacial electronic effect makes the catalytic surface favour the adsorption of electron-deficient reactants over electron-rich substrates (that is, *N*-hydroxylanilines), thus preventing full hydrogenation. More importantly, this interfacial electronic effect, achieved through simple organic modifications, may now be used for the optimization of commercial platinum catalysts.

Efficient and selective catalysts are important for the industrial production of commodity chemicals, as well as fine chemicals and pharmaceuticals[1,2]. To achieve high-yield production of target chemicals while avoiding the production of wastes, the development of highly selective catalysts has become an important focus in catalysis science[2,3]. In homogeneous catalysis and biocatalysis, ligands on catalytically active metal centres often induce significant steric and electronic effects that determine the overall selectivity of the catalysts[4–9]. Similarly, organic modifiers (ligands) on metal-based heterogeneous catalysts help to enhance the catalytic selectivity to some extent, mainly as a result of steric effects[10–13]. Limited success has been achieved in applying ligands to create electronic effects that determine the selectivity of heterogeneous metal catalysts, although the electronic effects of organic modifiers on their catalytic activities have been recently reported[14,15].

For heterogeneous metal catalysts, tuning the electronic structure has emerged as an important strategy to improve their performance. At present, there are the two main approaches to tune the electronic structure of heterogeneous metal nanocatalysts. One is to construct multimetallic nanoparticles that integrate metal components with different electronic properties. The other is to use supports to create strong metal–support interactions. For instance, fine control over the composition and structure of multimetallic nanocatalysts yields nanocatalysts with enhanced activity, selectivity and stability for oxygen reduction[16–21], the electrochemical reduction of CO_2 (ref. 22), the decomposition of formic acid[23], aerobic oxidation reactions[24,25] and so on[26]. The deposition of Pt nanoparticles on TiO_2 or CeO_2 creates water–gas shift catalysts with enhanced performance owing to the electronic perturbations between Pt and TiO_2 or CeO_2 (refs 27,28). In contrast to numerous studies on the electronic effects induced by inorganic components, little attention has been focused on the electronic effects induced by surface organic modifiers on heterogeneous catalysis[14,15]. Owing to the complexity of heterogeneous catalysts[29,30], understanding the electronic modulation due to organic modifiers is challenging, but it may lead to an effective and low-cost approach to optimize the catalytic performance of heterogeneous metal catalysts.

Here we demonstrate an interfacial electronic effect induced by simple organic modification to control the catalytic selectivity of Pt-based nanocatalysts in hydrogenation reactions. Such an interfacial effect leads to the catalytic production of the thermodynamically unfavourable but industrially important compounds *N*-hydroxylanilines, an important class of intermediates for many high-value products (Supplementary Fig. 1)[1,31–33]. At present, *N*-hydroxylanilines are mainly produced by the chemical reduction of nitroaromatics using expensive and environmentally unfriendly reducing agents (for example, zinc, hydrazine)[34,35]. It remains challenging to achieve the catalytically selective production of *N*-hydroxylanilines using low-cost and environmentally benign reducing agents. In this work, uniform ultrathin (~1.1 nm in diameter) Pt nanowires with ethylenediamine (EDA) chelated on their surfaces (denoted as EDA-Pt NWs) are chemically prepared and used as model nanocatalysts to elucidate the interfacial electronic effect induced by the interaction between EDA and Pt. In the hydrogenation of nitroaromatics, the as-prepared EDA-Pt NWs exhibit an unexpectedly high selectivity towards partially hydrogenated products, *N*-hydroxylanilines. Our study reveals that the electron donation from EDA to Pt NWs makes the surface of Pt NWs highly electron rich. During catalysis, such an interfacial electronic effect makes the Pt NWs favour the adsorption of electron-deficient reactants but disfavour the

[1]Collaborative Innovation Center of Chemistry for Energy Materials, State Key Laboratory for Physical Chemistry of Solid Surfaces, and Engineering Research Center for Nano-Preparation Technology of Fujian Province, Xiamen 361005, China. [2]National Engineering Laboratory for Green Chemical Productions of Alcohols–Ethers–Esters, College of Chemistry and Chemical Engineering, Xiamen University, Xiamen 361005, China. [3]Institute of Physics, Chinese Academy of Sciences, Beijing 100190, China. [4]State Key Laboratory of Molecular Reaction Dynamics, Dalian Institute of Chemical Physics, Chinese Academy of Sciences, Dalian 116023, China. †These authors contributed equally to this work. *e-mail: gfu@xmu.edu.cn; nfzheng@xmu.edu.cn

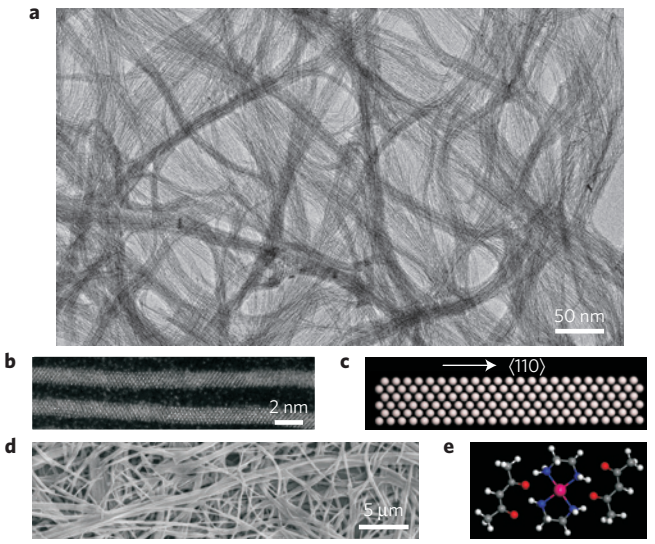

Figure 1 | Structure analysis of the ultrathin Pt NWs. a, A representative TEM image of large-scale Pt NWs. **b**, Sub-ångström-resolution high-angle annular dark-field (HAADF) STEM image of Pt NWs showing their uniform ultrathin features. **c**, Structure model showing the arrangement of Pt atoms in the ultrathin Pt NWs. **d**, SEM image of the $[Pt(EDA)_2](acac)_2$ intermediate for Pt nanowire preparation. **e**, Single-crystal structure of the $[Pt(EDA)_2](acac)_2$ intermediate. Colour codes: magenta, Pt; blue, N; red, O; grey, C; white, H.

adsorption of electron-rich substances (that is, *N*-hydroxylanilines), turning off the full hydrogenation. More importantly, the proposed interfacial electronic effect is experimentally confirmed by probing the binding strength and mode of adsorption of CO on Pt NWs. These simple organic modifications may therefore be applicable in optimizing the selectivity of commercial Pt catalysts.

Synthesis and characterization of EDA-coated Pt NWs

To prepare the ultrathin EDA-Pt NWs, Pt(II) acetylacetonate (acac) was thermally reduced in the presence of EDA in dimethylformamide (DMF) solution. Transmission electron microscopy (TEM) and aberration-corrected scanning transmission electron microscopy (STEM) revealed that uniform ultrathin Pt NWs were the dominant products (Fig. 1a and Supplementary Fig. 2). The diameter of Pt NWs averaged 1.1 nm, approximately 6–7 atoms thick, whereas their length was up to hundreds of nanometres. Despite their ultrathin nature, the as-prepared Pt NWs were highly crystalline (Fig. 1b). The selected-area Fourier transform analysis (Supplementary Fig. 3) indicated that Pt NWs had a face-centre-cubic (fcc) structure (Fig. 1c), consistent with the powder X-ray diffraction (XRD) pattern (Supplementary Fig. 4). A survey of tens of nanowires by high-resolution STEM (Fig. 1b) revealed that all the examined Pt NWs were single crystalline, with two types of clearly observed lattice fringes having interplanar spacings of 0.227 and 0.196 nm, ascribed to the 111 and 200 planes of fcc Pt.

Detailed studies revealed that the formation of a nanofibre intermediate with diameters of 50–150 nm (Fig. 1d and Supplementary Fig. 5) was critical for the successful preparation of the ultrathin Pt NWs. The nanofibre intermediate was a salt of the ionic $[Pt(EDA)_2](acac)_2$ complex with two EDA molecules chelated to one Pt(II), balanced by two acac anions, which was identified by X-ray single-structure analysis (Fig. 1e and Supplementary Table 1), X-ray powder diffraction, and elemental analysis (Supplementary Fig. 6). Owing to the poor solubility of $[Pt(EDA)_2](acac)_2$in DMF, Pt ions in the preformed intermediate nanofibres were confined therein for subsequent reductive formation of the ultrathin metallic Pt NWs. It is worth noting that the presence of 2 atm CO, a reducing and capping agent, was critical for the synthesis of uniform Pt NWs. The synthesis in the absence of CO led to the formation of short rods together with large nanoparticles (Supplementary Fig. 7). The presence of EDA on Pt NWs was confirmed by FTIR measurements (Supplementary Fig. 8a). As determined by thermogravimetric analysis (Supplementary Fig. 8b) and elemental analysis, the EDA coverage on Pt NWs was as high as 34.9 mol% over the total Pt atoms. Strong binding of EDA on the surface of Pt NWs was suggested by the temperature-programmed desorption-mass spectrometric profile, which revealed the decomposition of EDA above 200 °C (Supplementary Fig. 9). Moreover, the narrow and symmetric N1*s* X-ray photoelectron spectrum (XPS) (Supplementary Fig. 10) indicated the absence of multiple binding modes of EDA on Pt NWs.

High catalytic selectivity of Pt NWs

With their ultrathin diameter and well-modified surface, Pt NWs readily serve as a model nanocatalyst to demonstrate how organic modifiers control Pt catalysis. The selective hydrogenation of nitroaromatics was chosen because this is an important catalytic reaction towards high-value products (Supplementary Fig. 1a)[1,31–33] and at present it remains challenging to control product selectivity. Although Pt-based catalysts have been demonstrated as efficient catalysts for the hydrogenation of nitroaromatics, the end products resulting from Pt catalysts were mainly aniline derivatives[36–39]. DFT calculations demonstrated that nitrobenzene is hydrogenated to produce nitrosobenzene, *N*-hydroxylaniline and aniline successively, with reaction enthalpies (ΔH) of −0.93, −1.57 and −2.56 eV, respectively (Fig. 2a), consistent with previous analyses[40]. It is thus challenging to prevent the thermodynamically driven full hydrogenation and selectively produce partially hydrogenated products such as *N*-hydroxylanilines[41,42], which are industrially important chemicals (Supplementary Fig. 1b).

As evidenced by ^{1}H-NMR (Fig. 2b and Supplementary Fig. 11), when ultrathin EDA-Pt NWs were used as the catalyst in the room-temperature hydrogenation of nitrobenzene, *N*-hydroxylaniline was produced preferentially, with a nearly 100% selectivity within 50 min. Moreover, not much hydrogenation from *N*-hydroxylaniline to produce aniline was observed even when the reaction time was prolonged to 2 h (Fig. 2c). No significant decay in the selectivity was observed even after the catalyst was recycled five times. In the absence of additives, such a high selectivity to *N*-hydroxylaniline is unprecedented in conventional Pt catalysts. In contrast to EDA-Pt NWs, the commercial Pt black favoured full hydrogenation, leading to the formation of aniline as the main product. When nitrobenzene was fully converted, the yield of *N*-hydroxylaniline was only ∼33%. With the increased reaction time, *N*-hydroxylanilines were fully hydrogenated into anilines within 2 h (Fig. 2d). Reaction rate measurements confirmed that the hydrogenation of *N*-hydroxylaniline on EDA-Pt NWs was much slower than that on Pt black, although the hydrogenation of nitrobenzene occurred at a similar rate on both catalysts (Supplementary Fig. 12).

Moreover, an acid treatment removed part of the EDA on the Pt NWs (Supplementary Fig. 13) and was thus deleterious to the selectivity towards *N*-hydroxylaniline (83% at 100% conversion of nitrobenzene) (Supplementary Fig. 14). This result demonstrated the importance of EDA in achieving a high catalytic selectivity towards *N*-hydroxylaniline. Pt black after simple EDA treatment exhibited an enhanced selectivity to *N*-hydroxylaniline (74% at 100% conversion) (Supplementary Fig. 15). However, over both the acid-treated Pt NWs and EDA-treated Pt black, the selectivity of *N*-hydroxylaniline decreased markedly as the reaction time increased. These results strongly suggested that Pt NWs and EDA work in synergy to achieve the catalytic performance exhibited by EDA-Pt NWs.

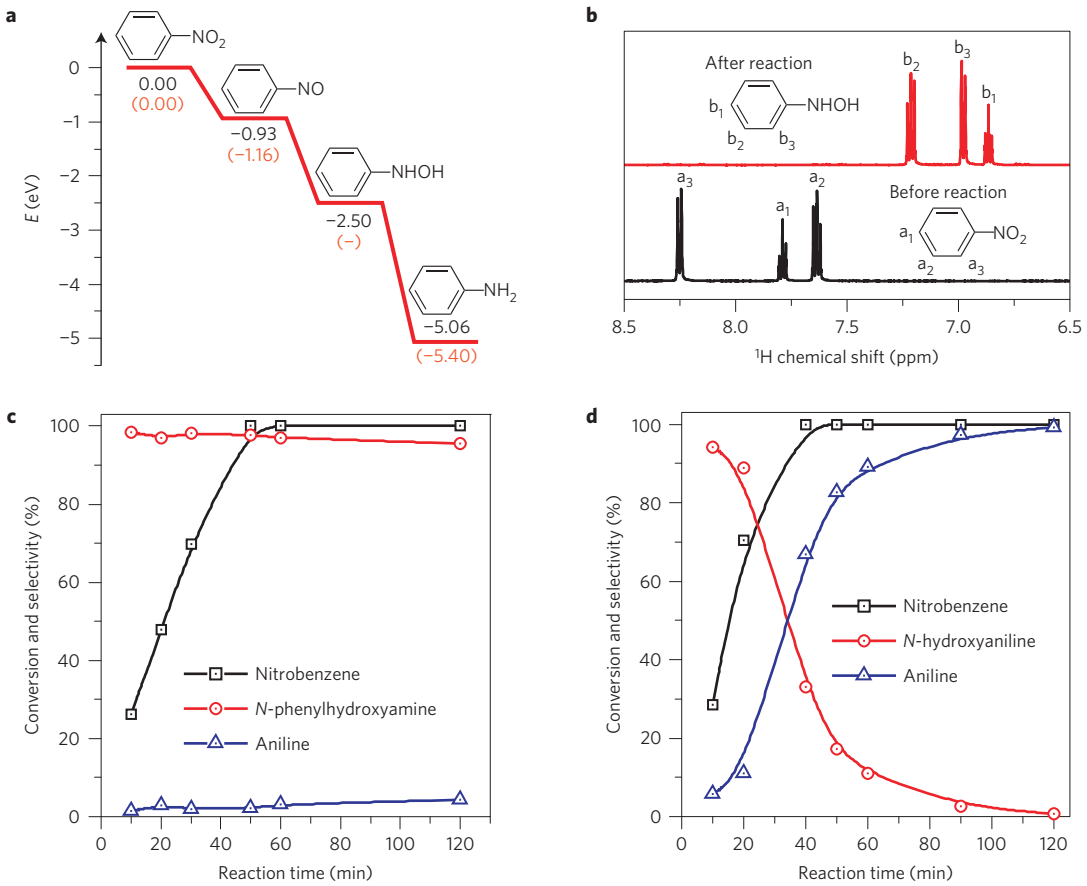

Figure 2 | Catalytic performance of EDA-Pt NWs. a, Stepwise hydrogenation of nitrobenzene and the corresponding energy profiles from DFT calculations (black) and ref. 40 (red). **b**, ^{1}H-NMR spectra for nitrobenzene hydrogenation reaction on Pt NWs after 50 min. Product (red) and reactant (black). **c**, Time-dependent catalysis by the EDA-Pt NWs. **d**, Time-dependent catalysis by commercial Pt black.

Mechanism of catalytic selectivity by Pt NWs

To understand how the EDA-Pt interface enhanced the catalytic selectivity, structural models of periodic Pt NWs (that is, both bare NWs and EDA-capped NWs) were built to simulate EDA-Pt NWs and optimized by using the Vienna *Ab initio* Simulation Package (VASP) code. In the optimized structure models (Fig. 3a and Supplementary Fig. 16), the nanowires have seven layers of Pt atoms, with a growth direction of [110], consistent with the high-resolution TEM (HRTEM) measurements. To simulate the surface roughness, 50% Pt atoms at the edges of the Pt NW were removed, resulting in 12 low-coordinated Pt atoms in every repeating unit containing 136 Pt atoms. Such a structure allowed 12 EDA molecules to be adsorbed in the chelating mode. As shown in Fig. 3b, the simulated EXAFS spectrum based on the optimized EDA-coated structure exhibited a distinct Pt–N peak similar to the experimental peak.

DFT calculations showed that the adsorption of EDA was very strong, with an average adsorption energy of −1.60 eV. With lone-pair electrons on N atoms, EDA molecules would donate their electrons to Pt NW on adsorption. The Bader charge analysis revealed that the uncovered surface atoms of EDA-Pt NW are negatively charged by −6.65 a.u. (−0.14 a.u./Pt atom), whereas the Pt atoms in the core are nearly neutral (+0.02 a.u./Pt atom). As shown in the cross-sectional profiles of Pt NWs (Fig. 3a), the charges of core Pt atoms were nearly unchanged with or without EDA chelating, whereas the donated electrons were mostly located on surface, especially around EDA-coordinated Pt atoms (Supplementary Fig. 17). Such an effect can be referred to as the interfacial electronic effect. To confirm this, XPS was performed to probe the change in the binding energy of Pt. Probably owing to the average effect of both the surface and core atoms, no obvious shift in the binding energy of Pt_{4f} from that of Pt(0) was revealed on EDA-Pt NWs (Supplementary Fig. 18). We thus shifted our efforts to CO stripping voltammetry, an effective technique to determine the surface electronic structure of noble metals[15]. Surprisingly, the CO stripping potential on EDA-Pt NWs was measured to be 0.83 V versus reversible hydrogen electrode (RHE), 0.22 V higher than that on Pt black (0.61 V versus RHE) (Fig. 3c). These results indicated that, following EDA adsorption, the surface of Pt NWs became electron rich and donated more electrons to CO $2\pi^*$ orbitals, thus strengthening CO adsorption and weakening C–O bonds. DFT calculations (Supplementary Table 2) confirmed that CO indeed carried a greater negative charge, and the CO adsorption on EDA-Pt NWs was enhanced. Moreover, as revealed by *in situ* electrochemical FTIR reflection spectroscopic studies (Fig. 3d and Supplementary Fig. 19), EDA-Pt NWs exhibited different CO binding strengths and adsorption sites from those of Pt black. The linear CO vibrational frequency on EDA-Pt NWs was 2,027 cm^{-1} at 0.1 V (versus RHE), 31 cm^{-1} lower than that on Pt black. Furthermore, the bridge adsorption of CO at 1,887 cm^{-1} on EDA-Pt NWs was even much stronger than the linear adsorption[43]. The change in CO binding was also confirmed by our calculations (Supplementary Table 2). CO adsorption on bridge and hollow sites benefited more from the electron-rich surface than that on the top sites. All these findings indicated that the chelating adsorption of EDA indeed altered the electronic state on the surface of Pt NWs.

Moreover, the catalytic selectivity of the Pt NWs was directly correlated with their surface electronic state. When part of the

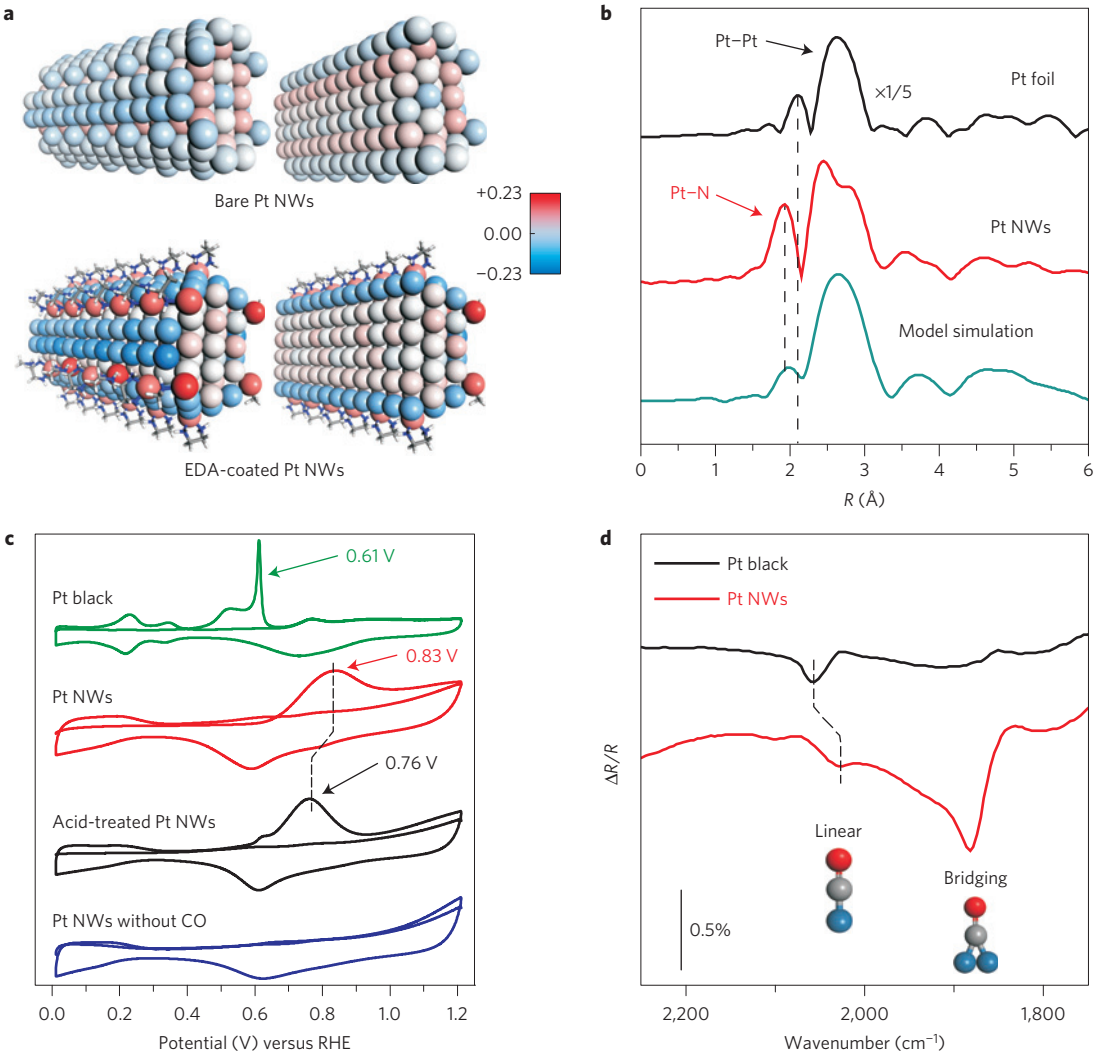

Figure 3 | The surface electronic effect induced by EDA. a, Constructed models of bare Pt NW and EDA-Pt NW and their corresponding Bader charge analysis. The colours in Pt NWs indicate the Bader charge of each atom. The profiles of each Pt NWs are shown on the left. **b**, The k^3-weighted Fourier transform spectra from EXAFS. $\Delta k = 2.5$–12.5 Å^{-1} are used for all the samples. The peak at ~1.7 Å in the first shell of Pt NWs is contributed by the interaction between Pt and EDA. Green line is the simulated result based on the optimized model of an EDA-coated Pt nanowire. **c**, CO stripping voltammetry of Pt black, EDA-Pt NWs, sulphuric acid (1 M) treated EDA-Pt NWs and EDA-Pt NWs without CO. **d**, *In situ* FTIR spectra for CO adsorbed on Pt black and EDA-Pt NWs, respectively, in 0.1 M NaOH solution at a potential of 0.1 V (versus RHE).

EDA on Pt NWs was removed by acid treatment, the CO stripping potential on Pt NWs was shifted to a lower potential (0.76 V versus RHE) (Fig. 3c), and the selectivity of acid-treated Pt NWs was consequently reduced to only 83%. Also, the CO stripping potential of EDA-treated Pt black was only 0.01 V (versus RHE) higher than that of pure Pt black (Supplementary Fig. 20). Accordingly, the enhancement in the selectivity to *N*-hydroxylaniline achieved by EDA-treated Pt black (Supplementary Fig. 15) was not as significant as that by EDA-Pt NWs.

Based on the above findings, we expected that the electron-rich nature of EDA-Pt NWs would alter the adsorption behaviour of *N*-containing aromatics. According to our DFT calculations, the adsorption free energies (ΔG_{ads}) of nitrobenzene, nitrosobenzene and *N*-hydroxylaniline on bare Pt NWs are −1.27, −1.48 and −0.89 eV, respectively (Supplementary Table 3), similar to those on low-Miller-index facets (Supplementary Table 4). This indicated that all of these *N*-containing aromatics are readily adsorbed on the pristine Pt catalysts to undergo hydrogenation after H_2 uptake, explaining the poor selectivity for *N*-hydroxylaniline of Pt black. However, when the Pt NW is chelated by 12 EDA, the remaining surface Pt atoms become inaccessible for *N*-containing aromatics as a result of steric effects. The adsorption of the substrates to be hydrogenated should compete with the pre-adsorbed EDA on Pt NWs to initiate the catalysis (Supplementary Table 3). Computationally, two possible mechanisms were considered, namely exchange and pull-and-occupy mechanisms. In the exchange mechanism, once the aromatics adsorbed on the low-coordinated Pt sites, EDA would be removed from the surface. In the pull-and-occupy mechanism, the adsorbed aromatics pull the EDA molecules to the vicinal sites, and occupy the low-coordinated sites. During this process, the adsorption of EDA would change from the chelating mode to the single-coordinated mode. We used ΔG_{ex} and ΔG_{po} instead of ΔG_{ads} to describe the feasibility of adsorption of an *N*-containing aromatic (Supplementary Figs 21 and 22).

As shown in Fig. 4a, ΔG_{po} for nitrobenzene and nitrosobenzene were calculated to be −0.55 and −0.87 eV, respectively, whereas ΔG_{po} for *N*-hydroxylaniline was 0.41 eV. A similar trend was obtained from ΔG_{ex} calculations. Even when Pt NWs were heavily coated by EDA, the adsorption of nitrobenzene or nitrosobenzene

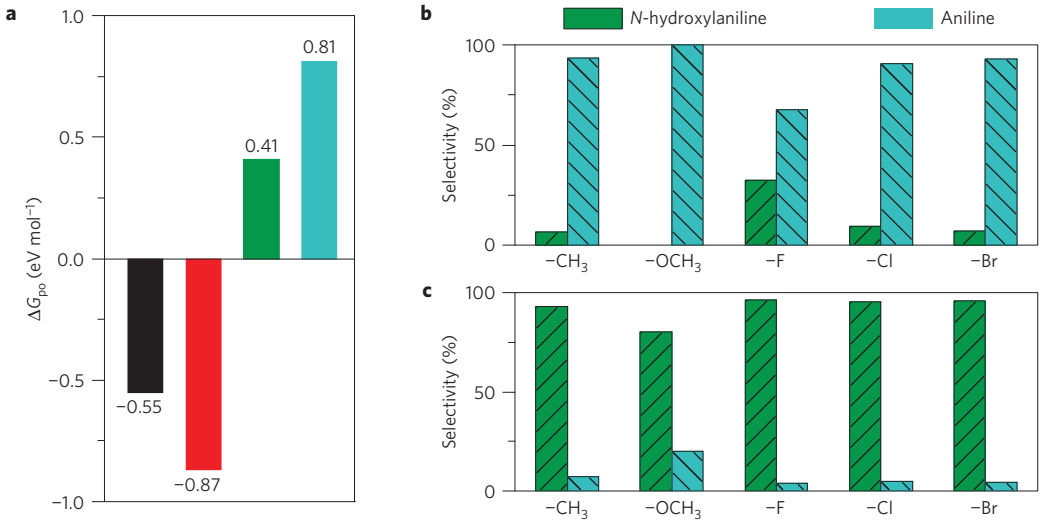

Figure 4 | Mechanism of catalytic selectivity of EDA-Pt NWs. a, Free energies (ΔG_{po}) for the adsorption of *N*-containing aromatics over EDA pre-coated Pt NWs. Black, nitrobenzene; red, nitrosobenzene; green, *N*-hydroxylaniline; blue, aniline. **b**,**c**, Comparison of the catalytic performances for the hydrogenation of substituted nitrobenzene over the commercial Pt black before (**b**) and after (**c**) Pt $(EDA)_2(acac)_2$ modification. Reaction conditions: methanol, 10 ml; solution of sodium hydroxide, 0.5 ml (1 M); substrate/metal molar ratio, 500; H_2, 0.05 MPa; temperature, 25 °C.

was feasible, whereas *N*-hydroxylaniline was still unable to access the surface of EDA-Pt NWs. However, for the adsorption of nitrobenzene or nitrosobenzene, the exchange mechanism was less favourable than the pull-and-occupy mechanism by ~0.2 eV (Supplementary Table 3). These results suggested that the selective catalysis might proceed without displacing EDA on Pt NWs, consistent with the fact that no detachment of EDA from Pt nanowires was detected during catalysis. As compared with bare Pt NWs, the adsorption free energies of nitrobenzene, nitrosobenzene and *N*-hydroxylaniline on the EDA-decorated Pt NWs were weakened by 0.72, 0.61 and 1.30 eV, respectively (Supplementary Table 3). Such changes in free energy can be understood in terms of the change in the spatial distribution of the electronic density(Supplementary Fig. 23). In the presence of EDA, *d* orbitals of Pt are nearly fully occupied, which favours the adsorption of electron-deficient substrates through d–π^* donation, but disfavours electron-rich substrates because the negatively charged Pt surface would pull more electrons into Pt···N antibonding states. The adsorption of nitrobenzene on EDA-Pt NWs was experimentally confirmed (Supplementary Fig. 24). The interfacial electronic effect on the catalytic selectivity observed in this work was afforded by tuning the adsorption energies of the substrates to be catalysed on Pt NWs. The electron-rich surface created by the interfacial electronic effect allows the selective hydrogenation of electron-deficient nitrobenzene and nitrosobenzene, but disfavours the adsorption of electron-rich *N*-hydroxylaniline. The extremely high selectivity towards *N*-hydroxylaniline achieved by EDA-Pt NWs mainly originates from the unique EDA-Pt interface rather than the ultrathin nature of Pt NWs. Nevertheless, the ultrathin feature plays an important role in providing abundant low-coordinated sites for EDA adsorption, thus reinforcing the interfacial electronic effect.

Application of interfacial electronic effect

With this understanding of how the chelating adsorption of EDA on Pt NWs enhances the catalytic selectivity, we attempted to apply the interfacial electronic effect to improve the selectivity of commercial Pt catalysts. Pt black was treated with $[Pt(EDA)_2](acac)_2$ to allow the deposition of Pt-EDA chelating units on its surface. As expected, the modified Pt black catalyst exhibited a high selectivity to *N*-hydroxylaniline (>97%) (Supplementary Fig. 25), and no obvious morphology change was observed after the modification (Supplementary Fig. 26). To further demonstrate the general applicability of the modified Pt catalyst, a series of nitroaromatics with various substitutions (that is, 1-fluoro-4-nitrobenzene, 1-chloro-4-nitrobenzene, 1-bromo-4-nitrobenzene, 1-methyl-4-nitrobenzene and 1-methoxy-4-nitrobenzene) were examined (Supplementary Fig. 27). As compared with the unmodified catalyst (Fig. 4b and Supplementary Fig. 28), the modified Pt black exhibited significantly enhanced selectivities towards the *N*-hydroxylaniline derivatives (Fig. 4c). Over the modified catalyst, the selectivities to *N*-hydroxylanilines at 100% conversion were 96.4%, 95.2%, 95.9%, 92.7% and 80% for –F, –Cl, –Br, $-CH_3$ and $-OCH_3$ substituted nitroaromatics, respectively. In comparison, under the same conditions, the unmodified catalyst gave the selectivities of only 32.4%, 9.6%, 6.9%, 6.5% and 0% respectively (Fig. 4b).

Our findings clearly demonstrate that organic surface modification offers an effective strategy to alter the electronic structure of metal nanocatalysts to optimize their catalytic performance. Modifying the surface of metal catalysts with organic ligands possessing different electronic and steric properties is expected to provide a powerful means to reinforce and enrich the interfacial electronic effect by coupling with the steric effect. The organic modification strategy developed not only provides a new research direction in engineering efficient metal nanocatalysts for fine chemical industries, but also extends our understanding of the coordination chemistry of nanocrystal surfaces[44].

Methods

Methods and any associated references are available in the online version of the paper.

Received 5 July 2015; accepted 22 December 2015; published online 25 January 2016

References

1. Sheldon, R. A. & Van Bekkum, H. *Fine Chemicals Through Heterogeneous Catalysis* (John Wiley, 2008).
2. Noyori, R. Synthesizing our future. *Nature Chem.* **1,** 5–6 (2009).
3. Somorjai, G. A. & Rioux, R. M. High technology catalysts towards 100% selectivity fabrication, characterization and reaction studies. *Catal. Today* **100,** 201–215 (2005).
4. Van Leeuwen, P. W. *Homogeneous Catalysis: Understanding the Art* (Springer Science Business Media, 2006).

5. Schmid, A. *et al*. Industrial biocatalysis today and tomorrow. *Nature* **409,** 258–268 (2001).
6. Rod, T. H. & Norskov, J. K. The surface science of enzymes. *Surf. Sci.* **500,** 678–698 (2002).
7. Wang, D.-H., Engle, K. M., Shi, B.-F. & Yu, J.-Q. Ligand-enabled reactivity and selectivity in a synthetically versatile aryl C–H olefination. *Science* **327,** 315–319 (2010).
8. Swiegers, G. F. *Mechanical Catalysis: Methods of Enzymatic, Homogeneous, and Heterogeneous Catalysis* (John Wiley, 2008).
9. Bhaduri, S. & Mukesh, D. *Homogeneous Catalysis: Mechanisms and Industrial Applications* (Wiley, 2000).
10. Marshall, S. T. *et al*. Controlled selectivity for palladium catalysts using self-assembled monolayers. *Nature Mater.* **9,** 853–858 (2010).
11. Astruc, D., Lu, F. & Aranzaes, J. R. Nanoparticles as recyclable catalysts. The frontier between homogeneous and heterogeneous catalysis. *Angew. Chem. Int. Ed.* **44,** 7852–7872 (2005).
12. Wu, B. H. & Zheng, N. F. Surface and interface control of noble metal nanocrystals for catalytic and electrocatalytic applications. *Nano Today* **8,** 168–197 (2013).
13. Medlin, J. W. Controlling selectivity in heterogeneous catalysis with organic modifiers. *Acc. Chem. Res.* **47,** 1438–1445 (2013).
14. Jones, S., Qu, J., Tedsree, K., Gong, X.-Q. & Tsang, S. C. E. Prominent electronic and geometric modifications of palladium nanoparticles by polymer stabilizers for hydrogen production under ambient conditions. *Angew. Chem. Int. Ed.* **51,** 11275–11278 (2012).
15. Luksirikul, P., Tedsree, K., Moloney, M. G., Green, M. L. H. & Tsang, S. C. E. Electron promotion by surface functional groups of single wall carbon nanotubes to overlying metal particles in a fuel-cell catalyst. *Angew. Chem. Int. Ed.* **51,** 6998–7001 (2012).
16. Stamenkovic, V. *et al*. Changing the activity of electrocatalysts for oxygen reduction by tuning the surface electronic structure. *Angew. Chem. Int. Ed.* **45,** 2897–2901 (2006).
17. Stamenkovic, V. R. *et al*. Improved oxygen reduction activity on $Pt_3Ni(111)$ via increased surface site availability. *Science* **315,** 493–497 (2007).
18. Zhang, J., Sasaki, K., Sutter, E. & Adzic, R. R. Stabilization of platinum oxygen-reduction electrocatalysts using gold clusters. *Science* **315,** 220–222 (2007).
19. Chen, C. *et al*. Highly crystalline multimetallic nanoframes with three-dimensional electrocatalytic surfaces. *Science* **343,** 1339–1343 (2014).
20. Cui, C. *et al*. Octahedral PtNi nanoparticle catalysts: exceptional oxygen reduction activity by tuning the alloy particle surface composition. *Nano Lett.* **12,** 5885–5889 (2012).
21. Strasser, P. *et al*. Lattice-strain control of the activity in dealloyed core-shell fuel cell catalysts. *Nature Chem.* **2,** 454–460 (2010).
22. Kim, D., Resasco, J., Yu, Y., Asiri, A. M. & Yang, P. Synergistic geometric and electronic effects for electrochemical reduction of carbon dioxide using gold–copper bimetallic nanoparticles. *Nature Commun.* **5,** 4948 (2014).
23. Tedsree, K. *et al*. Hydrogen production from formic acid decomposition at room temperature using a Ag–Pd core-shell nanocatalyst. *Nature Nanotech.* **6,** 302–307 (2011).
24. Enache, D. I. *et al*. Solvent-free oxidation of primary alcohols to aldehydes using $Au–Pd/TiO_2$ catalysts. *Science* **311,** 362–365 (2006).
25. Zhang, H., Watanabe, T., Okumura, M., Haruta, M. & Toshima, N. Catalytically highly active top gold atom on palladium nanocluster. *Nature Mater.* **11,** 49–52 (2012).
26. Chan, C. W. A. *et al*. Interstitial modification of palladium nanoparticles with boron atoms as a green catalyst for selective hydrogenation. *Nature Commun.* **5,** 5787 (2014).
27. Vayssilov, G. N. *et al*. Support nanostructure boosts oxygen transfer to catalytically active platinum nanoparticles. *Nature Mater.* **10,** 310–315 (2011).
28. Campbell, C. T. Catalyst-support interactions: electronic perturbations. *Nature Chem.* **4,** 597–598 (2012).
29. Bell, A. T. The impact of nanoscience on heterogeneous catalysis. *Science* **299,** 1688–1691 (2003).
30. Ross, J. R. *Heterogeneous Catalysis: Fundamentals and Applications* (Elsevier, 2012).
31. Blaser, H.-U. A golden boost to an old reaction. *Science* **313,** 312–313 (2006).
32. Corma, A. & Serna, P. Chemoselective hydrogenation of nitro compounds with supported gold catalysts. *Science* **313,** 332–334 (2006).
33. Solomina, T. A. *et al*. Prospects of catalytic reduction of aromatic nitro compounds by hydrogen. *Int. J. Hydrog. Energy* **20,** 159–161 (1995).
34. Bordwell, F. G. & Liu, W.-Z. Equilibrium acidities and homolytic bond dissociation energies of N–H and/or O–H bonds in *N*-phenylhydroxylamine and its derivatives. *J. Am. Chem. Soc.* **118,** 8777–8781 (1996).
35. Evans, D. A., Song, H.-J. & Fandrick, K. R. Enantioselective nitrone cycloadditions of alpha,beta-unsaturated 2-acyl imidazoles catalyzed by bis(oxazolinyl)pyridine-cerium(IV) triflate complexes. *Org. Lett.* **8,** 3351–3354 (2006).
36. Sun, Z. Y. *et al*. The solvent-free selective hydrogenation of nitrobenzene to aniline: an unexpected catalytic activity of ultrafine Pt nanoparticles deposited on carbon nanotubes. *Green Chem.* **12,** 1007–1011 (2010).
37. Corma, A., Serna, P., Concepcion, P. & Calvino, J. J. Transforming nonselective into chemoselective metal catalysts for the hydrogenation of substituted nitroaromatics. *J. Am. Chem. Soc.* **130,** 8748–8753 (2008).
38. Möbus, K. *et al*. Hydrogenation of aromatic nitrogroups with precious metal powder catalysts: influence of modifier on selectivity and activity. *Top. Catal.* **53,** 1126–1131 (2010).
39. Takasaki, M. *et al*. Chemoselective hydrogenation of nitroarenes with carbon nanofiber-supported platinum and palladium nanoparticles. *Org. Lett.* **10,** 1601–1604 (2008).
40. Linstrom, P. J. & Mallard, W. G. (eds) *NIST Chemistry WebBook, NIST Standard Reference Database Number 69* (National Institute of Standards and Technology, 19 December 2015); http://webbook.nist.gov
41. Oxley, P. W., Adger, B. M., Sasse, M. J. & Forth, M. A. *N*-acetyl-*N*-phenylhydroxylamine via catalytic transfer hydrogenation of nitrobenzene using hydrazine and rhodium on carbon. *Org. Synth.* http://doi.org/bmp73h (2003).
42. Takenaka, Y., Kiyosu, T., Choi, J.-C., Sakakura, T. & Yasuda, H. Selective synthesis of N-aryl hydroxylamines by the hydrogenation of nitroaromatics using supported platinum catalysts. *Green Chem.* **11,** 1385–1390 (2009).
43. Kinomoto, Y., Watanabe, S., Takahashi, M. & Ito, M. Infrared spectra of CO adsorbed on Pt(100), Pt(111), and Pt(110) electrode surfaces. *Surf. Sci.* **242,** 538–543 (1991).
44. Owen, J. The coordination chemistry of nanocrystal surfaces. *Science* **347,** 615–616 (2015).

Acknowledgements

We thank the MOST of China (2015CB932303), the NSFC (21420102001, 21131005, 21390390, 21333008, 21373167, 21133004), IRT_14R31, and the NFFTBS (J1210014) for the financial support. We thank Y. P. Zheng for help with XPS measurements, S. Q. Wei for preliminary XAS tests, Y. Ding and Z. L. Wang for preliminary HRTEM measurements. We also thank L. S. Zheng, Z. Q. Tian, L. W. Ye., M. S. Chen, B. Ren, J. F. Li, P. Zhang, Y. Zhao, J. Yang and P. N. Duchesne for helpful discussions.

Author contributions

N.Z. conceived the research project. G.C., C.X., X.H., Z.Z. and B.W. designed and synthesized the nanomaterials and carried out the catalysis experiments. G.F. carried out the model construction and DFT calculations. G.L. and Z.T. performed the TPD-MS experiments. J.Y. and Z.Z. carried out the *in situ* FTIR spectroscopy experiments. L.G. performed the HRTEM measurements. H.Y. performed the single-crystal analysis. All the authors contributed to the data analysis and drafted the manuscript.

Additional information

Supplementary information is available in the online version of the paper. Reprints and permissions information is available online at www.nature.com/reprints. Crystallographic data for this paper has been deposited at the Cambridge Crystallographic Data Centre under deposition number CCDC 1443564. Correspondence and requests for materials should be addressed to G.F. or N.Z.

Competing financial interests

The authors declare no competing financial interests.

Methods

Reagents. Pt(II) acetylacetonate [$Pt(acac)_2$] (99%) was purchased from Sino-Platinum Metals. Ethylenediamine (EDA), *N,N*-dimethylformamide (DMF), methanol, ethanol, sodium hydroxide (NaOH) and nitrobenzene were purchased from Sinopharm Chemical Reagent. CO (99.99%) and hydrogen (H_2) were purchased from Linde Industrial Gases. Pt black (~20 nm) was purchased from Sigma-Aldrich. Water used in all experiments was ultrapure (resistivity < 18.2 MΩ cm^{-1}). All reagents were used as received without further purification.

Synthesis of ultrathin Pt nanowires. $Pt(acac)_2$ (40.0 mg) and ethylenediamine (1 ml) were mixed together with *N,N*-dimethylformamide (10 ml) to get a homogeneous solution. The resulting light yellow solution was transferred to a glass pressure vessel. After charging with CO to 0.2 MPa, the vessel was heated from room temperature to 150 °C in 0.5 h and kept at this temperature for 5 h. The resulting colloidal products were collected by centrifugation, and then washed several times with ethanol. Before catalysis, CO adsorbed on the surface of Pt NWs was removed by exposing the Pt NWs in air.

Preparation of nanofibre intermediate $[Pt(EDA)_2](acac)_2$. $Pt(acac)_2$ (40.0 mg) and ethylenediamine (1 ml) were mixed together with *N,N*-dimethylformamide (10 ml) to get a homogeneous solution. The resulting homogeneous light yellow solution was transferred to a glass pressure vessel. After charging with CO to 0.2 MPa, the vessel was heated from room temperature to 120 °C with a heating rate of 4 °C min^{-1}. When the temperature reached 120 °C, the reaction was stopped immediately and cooled to room temperature. The as-prepared reaction intermediate was separated via centrifugation, washed with ethanol three times and then dispersed in 10 ml DMF.

$[Pt(EDA)_2](acac)_2$ modified commercial Pt black. 10.0 mg commercial Pt black and 9 ml DMF were mixed together with 0.5 ml water, and 0.5 ml of the as-prepared intermediate solution. The obtained mixture was transferred to a glass pressure vessel and sealed with a Teflon plug. The vessel was heated from room temperature to 150 °C with a heating rate of 4 °C min^{-1} and kept at this temperature for 5 h. The modified Pt black was washed with ethanol several times.

EDA-treated commercial Pt black. 10.0 mg Pt black was dispersed in 2.0 ml anhydrous EDA and consequently sonicated for 5 min. The treated Pt black was used in catalysis after washing in absolute ethanol four times. Before characterization, the Pt black was dried in a vacuum oven at room temperature overnight.

General procedure for the hydrogenation catalysis of nitroaromatics. In a reaction, 0.13 mg Pt nanowire, 1.0 mmol nitroaromatics, 0.5 ml NaOH (1 M) aqueous solution, methanol (10 ml) and ethanol (55 μl, as internal standard) were mixed together in a glass pressure vessel. The vessel was purged with H_2 to remove air from the reaction system before the catalytic reaction. The vessel was then pressurized with H_2 to 0.05 MPa. During the catalytic experiment, the pressure of H_2 was maintained constant. The catalytic products produced at different reaction times were investigated by ^{1}H-NMR. The NMR tubes were purged with argon before sample injection because *N*-hydroxylaniline was unstable in air. For the control experiments, all the reactions were performed with the same processes but with different catalysts.

Detection of possible detachment of EDA during catalysis. To detect possible replacement of EDA by nitrobenzene, 6.0 mg Pt NWs, 5 ml methanol, 0.25 NaOH (1 M) and 0.1 ml nitrobenzene were mixed together in a glass pressure vessel with vigorous stirring at room temperature for 1 h. To allow easier detection of the EDA detached from the Pt NWs, the amount of Pt NWs used in this study was 6.0 mg, ~45 times higher than that used in the measurement of the catalytic performance. The total concentration of EDA on the surface of Pt NWs was more than 81 ppm. The detection of EDA was performed on a GCMS-QP2010 Plus (SHIMADZU), which has a detection limit of 5 ppb.

Characterization. TEM studies were conducted on a TECNAI F-20 high-resolution transmission electron microscope operating at 200 kV. HRTEM measurements were carried out on an atomic-resolution analytical microscope (JEM-ARM 200F) operating at 200 kV. The samples were prepared by dropping ethanol dispersion of samples onto 300-mesh carbon-coated copper grids and immediately evaporating the solvent. X-ray diffraction (XRD) measurements were performed on a PANalytical X'pert PRO diffractometer using Cu Kα radiation, operating at 40 kV and 30 mA. Electrochemical measurements were carried out on a CHI760E electrochemical workstation (CH Instrument). X-ray photoelectron spectroscopy (XPS) measurements were carried out in an ultrahigh vacuum system using monochromatized Al Kα radiation (1,486.6 eV) and an Omicron Sphera II hemispherical electron energy analyser. Binding energies reported herein are with reference to C (1*s*) at 284.5 eV. ^{1}H-NMR spectra were recorded on an Advance III 500 MHz Unity plus spectrometer (Bruker) using residue solvent peaks as internal standards. The infrared spectra of the solid samples were recorded from 4,000 to 400 cm^{-1} on a Nicolet 380 FTIR spectrometer (Thermo Electron) using KBr pellets. Elemental analysis was performed on a Vario EL III(Germany). The thermogravimetric analysis (TGA) was performed on a TA SDT_Q600 analyser with a temperature ramping rate of 10 °C min^{-1} under a N_2 atmosphere.

Single-crystal analysis. The diffraction data of $[Pt(en)_2](acac)_2$ were collected on an Agilent Technologies SuperNova system X-ray single-crystal diffractometer with Mo Kα radiation ($\lambda = 0.71073$ Å) at 100 K. The data were processed using CrysAlis^{Pro} (ref. 45). The structure was solved and refined using the Full-matrix least-squares method based on F^2 with the programs ShelXT (ref. 46) and ShelXL (ref. 47) within Olex2 (ref. 48). Detailed crystallographic data are given in Supplementary Table 1.

Electrochemical measurements. The specific active surface areas (ECSAs) of all the catalysts (for example, Pt NWs, Pt black) were determined by measuring the areas under the hydrogen adsorption/desorption peaks of the cyclic voltammograms (CV) in an aqueous solution of 0.5 M H_2SO_4, assuming that a monolayer of H adatoms requires 210 μC cm^{-2}. To prepare a working electrode, an ethanol dispersion of purified catalysts (10 μg) was deposited on a glassy carbon electrode (4 mm). After the ethanol was dried, 5 μl of 2.5 V% Nafion solution was dropped on the electrode surface to stabilize the catalysts on the electrode surface. A saturated calomel electrode (SCE) and a platinum wire were used as the reference and counter electrode, respectively. Cycles of potential sweeps between 0 and 1.44 V (versus RHE) at a sweep rate of 100 mV s^{-1} were applied until the maximum electrochemical surface area (ECSA) was obtained. All the catalysts used in catalysis were based on the same ECSAs.

For CO stripping, pure CO gas was purged through the catalyst surface in the cells filled with 0.1 M KOH electrolyte for 15 min while holding the working electrode at 0.1 V (versus RHE). After transferring the electrodes to another cell filled with fresh 0.1 M KOH electrolyte (without CO), the CO stripping was performed in the potential range 0–1.2 V (versus RHE) at a scan rate of 20 mV s^{-1}.

Electrochemical *in situ* FTIR reflection spectroscopy. *In situ* FTIR spectroscopy experiments were carried out on a Nexus 870 FTIR spectrometer (Nicolet) equipped with a liquid-nitrogen-cooled mercury cadmium telluride MCT—A detector. A thin-layer *in situ* FTIR cell with CaF_2 window was utilized. A total of 400 single beams at a resolution of 4 cm^{-1} were co-added to increase the signal-to-noise ratio. The *in situ* FTIR spectra CO_{ad} was measured in 0.1 M NaOH solution using the following procedure: purge the electrolyte with N_2 for 15 min; hold the electrode at potential of 0.10 V (versus RHE) while bubbling bubbles of CO for 15 min; push the electrode to the window after removing the completely dissolved CO in solution by bubbling N_2; collect the sample spectra under a series of sample potentials (E_S); the reference spectrum is finally acquired at E_R (1.1 V for Pt NWs and 0.8 V for Pt black), at which the adsorbed CO is oxidized completely. The reference spectra were also acquired at 0.1 V for both Pt NWs and Pt black, at which the CO oxidation does not occur. The resulting spectra were reported as the relative change in reflectivity, given by

$$\frac{\Delta R}{R}(E_S) = \frac{R(E_S) - R(E_R)}{R(E_R)} \quad (1)$$

where $R(E_S)$ and $R(E_R)$ are single-beam spectra collected at the sample potential (E_S) and the reference potential (E_R), respectively.

Temperature-programmed desorption mass spectrometry (TPD-MS). The TPD-MS experiment was performed on an in-house-built TPD-TOF analyser. 2.0 mg of Pt NWs sample was pyrolysed in a small tube heated by heating coil. A K-type thermocouple was put inside the sample tube and insulated from the samples to measure the temperature. The heating coil was powered by a precise electric source and adjusted in intervals of 10 mV. The temperature of the sample tube was ramped from room temperature to 800 °C smoothly at a rate of 5 °C min^{-1} controlled by computer. The desorbed species were ionized by an ultraviolet lamp positioned very close to the sample tube with a photon energy of 10.6 eV, and then transferred to the TOF analyser by an ion optical system. The TOF analyser had a resolution of better than 5,000 and a sensitivity at the ppb level. All these steps were processed in a high vacuum (~3×10^{-5} Pa). The mass spectrum and sample temperature were acquired and recorded every second. Each spectrum is an accumulation of 10,000 spectra gathered at intervals of 100 μs.

X-ray absorption spectroscopy measurements. The X-ray absorption spectra at the Pt L_{III}-edge were recorded at the BL14W1 beamline in the Shanghai Synchrotron Radiation Facility (SSRF). The electron storage ring was operated at 35 GeV. Using a Si(111) double-crystal monochromator, all the data collections

were carried out in the transmission mode for the Pt L_{III}-edge. All spectra were collected in air at room temperature. A Pt foil (standard) was measured simultaneously and used for the energy calibration. The beam size was limited by horizontal and vertical slits with an area of $2 \times 2\,mm^2$ during the XAS measurements. The XAS data analysis was carried out with the programs of IFEFFIT.

Computational details. Periodic DFT calculations were performed using the Perdew–Burke–Ernzerhof (PBE; ref. 49) gradient-corrected exchange-corrected functional with the projector augmented plane wave (PAW; refs 50,51) method as implemented in the Vienna *Ab initio* Simulation Package (VASP; refs 52,53). The plane wave kinetic energy cutoff was set to 400 eV. During structural optimization, all atoms were fully relaxed until the residual forces were less than 0.03 eV $Å^{-1}$.

Through HRTEM analysis, the ultrathin Pt nanowire consists of 6–7 atomic layers with the growth direction of [110]. On this basis, a structural model with exposed facets of (100) and (111) was proposed. To simulate the surface roughness, 50% of the Pt atoms at the edges of the nanowire were removed, resulting in 12 five-coordinated Pt atoms on the surface. Such low-coordinated Pt sites allowed EDA adsorption in the chelating mode. To avoid interactions between the periodically repeated images, we put the model into a $30.0 \times 35.0 \times 10.9191\,Å^3$ unit cell and the k-points sampling was generated following the Monkhorst–Pack procedure with a $1 \times 1 \times 3$ mesh. The adsorption energy (ΔE_{ads}) of molecules can be defined as:

$$\Delta E_{ads} = E_{DFT(NW/mole)} - E_{DFT(NW)} - E_{DFT(mole)} \quad (2)$$

in which E_{DFT}(NW/mole) is the energy of the nanowire (EDA-free or coated with EDA) with adsorbates; E_{DFT}(NW) is the energy of the nanowire (with or without EDA coating); and E_{DFT} (mole) is the energy of an isolated molecule. As the reactions were in solution, the related Gibbs free energy at a given temperature can be defined as:

$$\Delta G_{ads} = \Delta G_{(NW/mole)} - \Delta G_{(NW)} - \mu_{(mole)} - \Delta G_{sol(Corr)} \quad (3)$$

The solid Gibbs free energies and solvent phase chemical potential can be written as

$$\Delta G_{(NW)} = H_0 - RTln(Q_{vib}) \quad (4)$$

$$\mu_{(mole)} = H - RTln(Q_{vib} \cdot Q_{rot} \cdot Q_{trans}) \quad (5)$$

where

$$H = E_{el} + E_{ZPE} \quad (6)$$

Here H_0 is the enthalpy at 0 K, which is equal to total electronic energy (E_{el}) plus the zero-point correction energy, E_{ZPE}, and Q_{vib}, Q_{rot} and Q_{trans} are the partition functions for vibration, rotation and translation, respectively, which can be obtained by using the Gaussian09 code[54]. In this case, the PBE functional combined with the 6-311+G(2*d*,2*p*) basis set was employed. Here, we neglected the internal vibrational contribution of the solid and assumed that E_{ZPE}, $RTlnQ_{vib}$ and $RTlnQ_{rot}$ would be the same whether molecules were in solution or adsorbed on the surface.

For reactions taking place in the solution, the cost associated with loss of translational degrees of freedom on adsorption was overestimated—that is, solvent cage effects. $\Delta G_{sol(Corr)}$ is a correction term for cage effects, which was estimated to be 2.54 kcal mol^{-1} for a bimolecular reaction in solution at 298 K (ref. 55).

Accordingly, equation (3) can be rewritten as

$$\Delta G_{ads} = \Delta E_{ads} + RTlnQ_{trans(mole)} - \Delta G_{sol(Corr)} \quad (7)$$

When *N*-containing aromatics adsorbed on the EDA-coated surface, we considered two possible adsorption mechanisms. The first mechanism is the exchange mechanism, in which once the aromatics adsorbed on the low-coordinated Pt site, the EDA would be fully displaced. The free energy of the exchange process (ΔG_{ex}) can be defined as:

$$\Delta G_{ex} = \Delta G_{ads(NW\text{-}11EDA/mole)} - \Delta G_{ads(NW\text{-}11EDA/EDA)} \quad (8)$$

Here, $\Delta G_{ads(NW\text{-}11EDA/mole)}$ stands for the free energy of adsorption on a Pt NW coated with 11 EDA; $\Delta G_{ads(NW\text{-}11EDA/EDA)}$ stands for the free energy of adsorption of the last EDA molecule.

Adsorption can also occur via the pull-and-occupy mechanism, in which the adsorbed aromatics can pull the EDA molecules to the vicinal sites, and occupy the low-coordinated sites. During the process, the adsorption of EDA would be changed from the chelating mode to the single-coordinated mode (viz. 'one leg' mode). The free energy of the pull-and-occupy process can be written as:

$$\Delta G_{po} = \Delta G_{ads(NW\text{-}12EDA/mole)} - \Delta G_{(NW\text{-}12EDA)} - \mu_{(mole)} - \Delta G_{sol(Corr)} \quad (9)$$

Here, $\Delta G_{ads(NW\text{-}12EDA/mole)}$ stands for the free energy of adsorption on a Pt NW coated with 12 EDA.

References

45. *CrysAlis Pro* Version 1.171.35.19 (Agilent Technologies, 2011).
46. Sheldrick, G. M. SHELXT-Integrated space-group and crystal-structure determination. *Acta Crystallogr. C* **71,** 3–8 (2015).
47. Sheldrick, G. M. A short history of SHELX. *Acta Crystallogr. A* **64,** 112–122 (2008).
48. Dolomanov, O. V., Bourhis, L. J., Gildea, R. J., Howard, J. A. & Puschmann, H. OLEX2: a complete structure solution, refinement and analysis program. *J. Appl. Crystallogr.* **42,** 339–341 (2009).
49. Perdew, J. P., Burke, K. & Ernzerhof, M. Generalized gradient approximation made simple. *Phys. Rev. Lett.* **77,** 3865–3868 (1996).
50. Blöchl, P. E. Projector augmented-wave method. *Phys. Rev. B* **50,** 17953–17979 (1994).
51. Kresse, G. & Joubert, D. From ultrasoft pseudopotentials to the projector augmented-wave method. *Phys. Rev. B* **59,** 1758–1775 (1999).
52. Kresse, G. & Furthmüller, J. Efficient iterative schemes for *ab initio* total-energy calculations using a plane-wave basis set. *Phys. Rev. B* **54,** 11169–11186 (1996).
53. Kresse, G. & Hafner, J. *Ab initio* molecular dynamics for open-shell transition metals. *Phys. Rev. B* **48,** 13115–13118 (1993).
54. Frisch, M. J. *et al*. *Gaussian 09,* Revision D.01 (Gaussian, 2009).
55. Galano, A. & Cruz-Torresb, A. OH radical reactions with phenylalanine in free and peptide forms. *Org. Biomol. Chem.* **6,** 732–738 (2008).